Background-free four-wave mixing microscopy of small gold nanoparticles inside a multi-cellular organ Ⓕ

Ⓘ Iestyn Pope, Ⓘ Nuno G. C. Ferreira, Ⓘ Peter Kille, et al.

COLLECTIONS

Note: This paper is part of the APL Special Collection on Advances in Optical Microscopy for Bioimaging.

Ⓕ This paper was selected as Featured

View Online   Export Citation   CrossMark

AIP Publishing

Background-free four-wave mixing microscopy of small gold nanoparticles inside a multi-cellular organ

View Online Export Citation CrossMark

Iestyn Pope,[1] (iD) Nuno G. C. Ferreira,[1,a)] (iD) Peter Kille,[1] (iD) Wolfgang Langbein,[2,b)] (iD) and Paola Borri[1] (iD)

AFFILIATIONS

[1] School of Biosciences, Cardiff University, Museum Avenue, Cardiff, CF10 3AX, United Kingdom
[2] School of Physics and Astronomy, Cardiff University, The Parade, Cardiff CF24 3AA, United Kingdom

Note: This paper is part of the APL Special Collection on Advances in Optical Microscopy for Bioimaging.
a) **Present address:** CIIMAR - Terminal de Cruzeiros de Leixões, Av. General Norton de Matos s/n, 4450-208 Matosinhos, Portugal.
b) **Author to whom correspondence should be addressed:** langbeinww@cardiff.ac.uk

ABSTRACT

The ability to detect small metallic nanoparticles by optical microscopy inside environmentally relevant species may have a wide impact for ecotoxicology studies. Here, we demonstrate four-wave mixing microscopy on individual small gold nanoparticles inside the hepatopancreas of *Oniscus Asellus*, a terrestrial isopod, which ingests metals found in the soil. After the exposure to food containing 10 nm radius gold nanoparticles, hepatopancreas tubules were collected, and nanoparticles were imaged by four-wave mixing microscopy with high contrast, locating them with sub-cellular resolution in the volume, despite the significant light scattering from these multi-cellular organs. Notably, the ultrafast dynamics of the four-wave-mixing non-linearity of gold nanoparticles resonantly excited and probed at their localized surface plasmon allows them to be distinguished from other metal deposits in the hepatopancreas, which manifest as a long-lived photothermal contrast. Our findings bring unexpected insight into the location of gold nanoparticles in relation to the cell types forming the hepatopancreas. Considering its simplicity, volumetric imaging capabilities, specificity, and compatibility with living cell studies, four-wave mixing microscopy holds great potential to investigate the fate of metal nanoparticles inside biological systems.

Metal nanoparticles (NPs) are ubiquitous in research and industrial applications and enter ecosystems, demanding a better understanding of their toxicity. Notably, the fate of these NPs inside cells of environmentally relevant organisms is still poorly understood due to the lack of microscopy techniques having the required three-dimensional (3D) spatial resolution, sensitivity, specificity, and applicability *in situ* ideally on the living specimen. A relevant method to map the chemical composition of metals inside biological cells with sub-micron resolution, high chemical specificity, and sensitivity to nanoparticle amounts is synchrotron-based x-ray fluorescence (XRF) microscopy.[1] While widely utilized in the fields of cellular toxicology, pharmacology, and metal-related biomedical research, this method is time consuming and expensive, requiring access to dedicated synchrotron beamline facilities. Moreover, XRF microscopy operates on fixed, thinly sectioned material; hence, it is not 3D and neither is it compatible with live cell imaging.

Recently, we have introduced an optical microscopy method able to detect single small (down to 5 nm radius) gold NPs (AuNPs) inside cells with high signal-to-noise ratio, free from light scattering and autofluorescence background, at useful speeds (0.1–1 ms per pixel) and low excitation powers ($<100\,\mu$W), compatible with live cell imaging.[2,3] The technique exploits the electronically resonant four-wave mixing (FWM) nonlinearity of AuNPs using a sequence of short optical pulses centered at the localized surface plasmon resonance (LSPR) of the AuNPs. This FWM microscopy method features spatial resolution better than the one-photon diffraction limit in 3D and optical sectioning of volumetric samples. Importantly, it can locate the position of a single AuNP with precision at the nanoscale inside complex 3D samples.[2–4]

Resonant FWM in our experiment can be understood as a pump-probe technique [see the sketch in Fig. 1(d)], whereby a pump pulse is optically absorbed, transferring its energy to electronic

excitations which rapidly (within a few hundreds of femtoseconds) form a hot electron gas in the metal.[5] Heating of the electron gas changes the dielectric function of gold, leading to broadening and shifting of the LSPR, modifying the AuNP light scattering, which is measured by the probe. By varying the arrival time of the probe pulse relative to the pump, the heating and subsequent cooling dynamics of the electron gas thermalizing with the lattice (on the tens of picoseconds timescale) can be measured. This characteristic ultrafast dynamics is, therefore, a specific response of AuNPs resonantly excited at the LSPR, separated from long-lived photo-thermal effects in the presence of other absorbing materials.

In this context, we study here the applicability of FWM microscopy to locate individual AuNPs in 3D inside the hepatopancreas (HP) of an environmentally important organism, namely, *Oniscus asellus* (the common woodlouse) and distinguish them from other absorbing metallic (Cu, Fe) materials known to be stored within organelles in this species. Woodlice can be found living in almost all terrestrial ecosystems and are a widely used organism in soil ecotoxicology. They are a detritivorous species that feeds on decaying organic matter and are part of the macrodecomposer community structure, mediating soil aeration and drainage and incorporating the organic matter back into the soil.[6,7] Importantly, these organisms can inhabit heavily metal-contaminated areas, ingesting metal NPs from the environment and achieving tolerance/resistance by accumulative immobilization.[8] As a result, these isopods are considered excellent model organisms by the biology community for mechanistic "metallomics." Notably, they exhibit processes such as environmental ion assimilation[9–11] and homeostatic metallo-sequestration,[12] which appear to target individual metals to highly specific cell types and into specific intra-cellular compartments.

In our study, we exposed a culture of *Oniscus asellus* to food spiked with 10 nm radius AuNPs in a gelatin matrix (see supplementary material Sec. S3 for details) and tested the 3D imaging capabilities of our FWM microscope to specifically distinguish and locate these small AuNPs intra-cellularly within the millimeter-long multi-cellular HP, which is the central organ involved in metal transport, accumulation, and detoxification in these organisms.[12]

A sketch of the FWM microscope is shown in supplementary material Fig. S1 and briefly explained in the following. We use optical pulses of 150 fs duration centered at 550 nm wavelength with $\nu_L = 80$ MHz repetition rate, provided by the signal output of an optical parametric oscillator, split into three beams, acting as a pump (E_1 field), a probe (E_2 field), and a reference. The pump intensity is amplitude modulated at $\nu_m = 0.4$ MHz. The probe pulse follows the pump with adjustable delay time τ. Pump and probe pulses are recombined and focused onto the sample by a high numerical aperture (NA) water-immersion objective mounted onto an inverted microscope stand. The sample is moved with respect to the focal volume of the objective by scanning an *xyz* sample stage with nanometric position precision. A FWM field proportional to $E_1 E_1^* E_2$ is collected by the same objective, together with the reflected probe field, and recombined with the reference pulse. The resulting interference is detected by balanced photodiodes. We use a heterodyne scheme to discriminate the FWM field from the pump and probe.[2] In this scheme, the probe optical frequency is upshifted by radio frequency amount ($\nu_2 = 82$ MHz), and the interference of FWM and probe fields with the unshifted reference is detected. As a result of the amplitude modulation of the pump

at ν_m, the frequency shift of the probe by ν_2, and the repetition rate ν_L of the pulse train, this interference gives rise to a beat note at $\nu_2 - \nu_L = 2$ MHz for the reflected probe, and sidebands at $\nu_2 \pm \nu_m - \nu_L = 2 \pm 0.4$ MHz for the FWM field, detected using a multi-channel lock-in amplifier. The balanced photodiodes use about 300 μW of the reference power per diode, providing about 100 μA photocurrent, and have a current amplifier of 10^5 V/A transimpedance. For the same signal power as reference power, namely, 600 μW, we obtain 400 μA maximum photocurrent for constructive interference. From these values and taking into account that the detected signal amplitude is a root-mean square voltage, we deduce a square voltage to power conversion factor of 0.19 μW/V^2. Typical reflected signals have amplitudes of 0.1 V, corresponding to 1.9 nW or 5.3×10^9 photons/s, while FWM signals have amplitudes of 0.5 mV, corresponding to 47 fW or 1.3×10^5 photons/s. During a pixel dwell time of 0.5 ms, 0.5 mV amplitude, thus, corresponds to 65 photons, providing a signal to noise ratio given by the square root of the number of photons of about 8, consistent with the data shown, confirming shot-noise limited detection.

The 3D spatial resolution of our FWM microscope was characterized previously.[3,4,13] For the objective lens used here, the spatial resolution is about 280 nm in the lateral direction and 740 nm in the axial direction given by the FWM field amplitude point spread function full-width-half-maximum. We also showed that the centroid localization precision for a single AuNP can be below 5 nm in 3D, depending on the signal-to-noise ratio in the experiment.[4]

Examples of FWM microscopy in the HP of an *Oniscus asellus* are shown in Figs. 1–3. As depicted in the sketch of Fig. 1(a), the HP consists of two pairs of helical tubules running the length of the body cavity situated either side of the centrally located hind gut with each tubule approximately 0.5 mm in diameter and a few mm in length. The tubules themselves contain two cell types: large "B" cells and smaller "S" cells. The smaller, cone shaped S cells have been shown to contain cuprosomes (Cu and S-rich organelles) that participate, for example, in hemocyanin synthesis, whereas the larger B cells contain Fe inclusions.[8] In addition, B cells undergo a diurnal cycle, where their rich carbohydrate and lipid content are released into the hepatopancreas. For our measurements, isopods were collected after 96 h exposure to food containing 10 nm radius AuNPs, and during the period where B cells are believed to be accumulating metals (phase before the nocturnal period). Two sample preparation procedures were followed. For the results in Figs. 1 and 2, the HP was dissected, and single tubules were mounted in water between a glass coverslip and a slide inside a 120 μm thick imaging gasket. Conversely, Fig. 3 shows HP tubules that were dissected and immediately embedded within proprietary cryo-moulds, frozen in liquid nitrogen, sectioned into 12 μm thick slices and mounted, embedded in water, inside a glass coverslip-slide sealed chamber (see Ref. 8 for details).

An overview image of the HP tubule is shown in Figs. 1(b) and 2(a) using bright-field transmission microscopy available on the FWM microscope (see supplementary material Sec. S2 for details), which exemplifies the length and helical structure. A zoom of the region of interest measured with FWM is highlighted [Fig. 1(c)]. Figures 1(e)–1(g) show a single plane *xy* FWM image from within the HP tubule. It compares results acquired at the pump-probe delay time $\tau = 0.5$ ps, where the FWM amplitude transiently reaches its
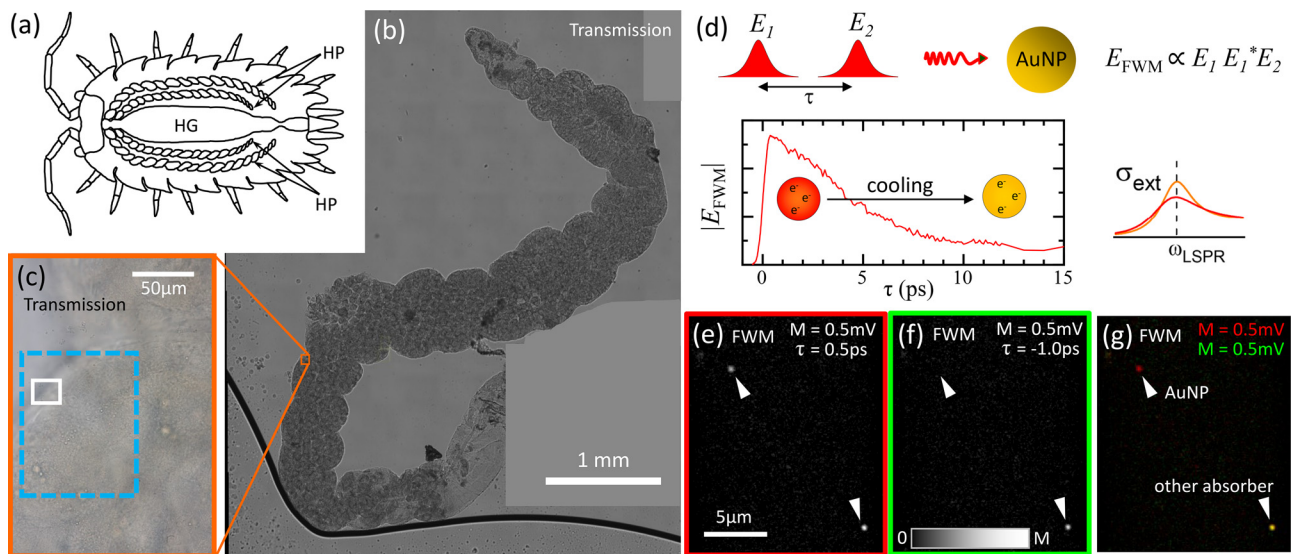
FIG. 1. (a) Cartoon of *Oniscus asellus* depicting the hepatopancreas (HP) and the hind gut (HG). (b) Stitched wide-field transmission overview (taken using a 10×0.3 NA dry objective) of a single HP tubule, showing the helical structure. (c) Higher magnification of the region highlighted by the orange frame in (b) taken with the 60×1.27 NA water-immersion objective also used for FWM, containing the regions imaged by FWM. The small white box indicates the region imaged by FWM in (e)–(g), and the dashed blue box the region imaged by FWM shown in Figs. 2(g)–2(j). Scale bar: $50\,\mu m$. (d) Sketch of the transient four-wave mixing process as a pump E_1 field–probe E_2 field technique using short optical pulses in resonance with the localized surface plasmon of the AuNP. The dynamics of the FWM field amplitude vs pump-probe delay time τ measured on a 10 nm radius AuNP is shown, together with a sketch of the optical extinction (σ_{ext}) spectrum of the AuNP, which is broadened and shifted upon absorption of the pump pulse and formation of a hot electron gas. (e) and (f) FWM microscopy of individual nanoparticles inside the HP at pump-probe delays of $\tau = 0.5$ ps (e) and $\tau = -1$ ps (f). Pump (probe) power at the sample was $60\,\mu W$ ($30\,\mu W$), 0.1 ms pixel dwell time, $16.4 \times 20\,\mu m^2$ image with 72 nm pixel size. Scale bar is $5\,\mu m$. Gray scale from 0 to M as given. (g) Color overlay of (d) in red and (e) in green.

maximum following the resonant excitation of the hot electron gas in the AuNP, and at $\tau = -1$ ps which shows a response due to long-lived changes induced by pump pulses in previous cycles of the pulse train 13 ns apart. An absorbing material can generate such a long-lived pump-induced change as a photo-thermal effect, namely, the absorbed pump energy converted into heat changes the temperature and in turn the refractive index of the surrounding medium, which modulates the reflected probe. A small photothermal contribution at negative delay times is visible in the curve showing the FWM amplitude dynamics vs τ for a 10 nm radius AuNP in Fig. 1(d). However, the resonant contribution due to the shift and broadening of the AuNP LSPR spectrum with maximum effect at $\tau = 0.5$ ps dominates. In Figs. 1(e)–1(g), two particles (indicated by arrows) can be seen. One of them shows the dynamics expected for a AuNP, while the other shows a long-lived photo-thermal response, with a FWM amplitude of comparable strength at $\tau = -1$ ps and $\tau = 0.5$ ps. This is highlighted by the red–green overlay of the images at positive–negative delay time, whereby the photo-thermal structure appears yellow and the AuNP is red.

Figure 2 shows 3D FWM data taken within the HP tubule, exemplifying the optical sectioning and background-free contrast of this microscopy method able to visualize a single small AuNP inside a highly scattering multicellular 3D organ. Probe reflection images acquired simultaneously with FWM images are provided for comparison, highlighting the significant light scattering from these tissues, in

which the AuNPs are not discernible even though they are excited at their LSPR. This is exemplified comparing the reflection in panel 2(c) with the FWM in panel 2(d)—clearly, the AuNP seen in Fig. 2(d) is not discernible in c. FWM z-stacks are shown as maximum amplitude projections in-plane (xy) in panel 2(i) and transversally (yz) in panel 2(j). Using red–green overlays as described above, the presence and location of AuNPs distinguished from photo-thermal structures are visible with high contrast. Again, corresponding reflection sections in panels 2(g) and 2(h) do not allow AuNPs to be distinguished. Considering that the HP of *Oniscus asellus* has been shown to store metals such as Cu and Fe within intracellular organelles and inclusions, it is likely that these metal structures are the source of the observed photo-thermal response.

To further investigate the location of AuNPs inside the HP especially in relation to the S and B cell types, HP tubules were sectioned, and the cell nuclei stained with the fluorescence dye DAPI to aid their identification, as B cells have a double nucleus[8] (see supplementary material Sec. S3 for details of sample preparation). Figure 3 shows an overview of this study. Differential interference contrast (DIC) microscopy and wide-field epifluorescence microscopy were carried out as a characterization of the stained section prior to FWM microscopy. (Details are given in supplementary material Sec. S2.) A DIC image (gray scale) overlayed with the wide field fluorescence image of the nuclei stain (blue) is shown in Fig. 3(a). Cells are attributed to S or B type using their size, shape, and number of nuclei and indicated by black and white arrows, respectively. We note that B cells are
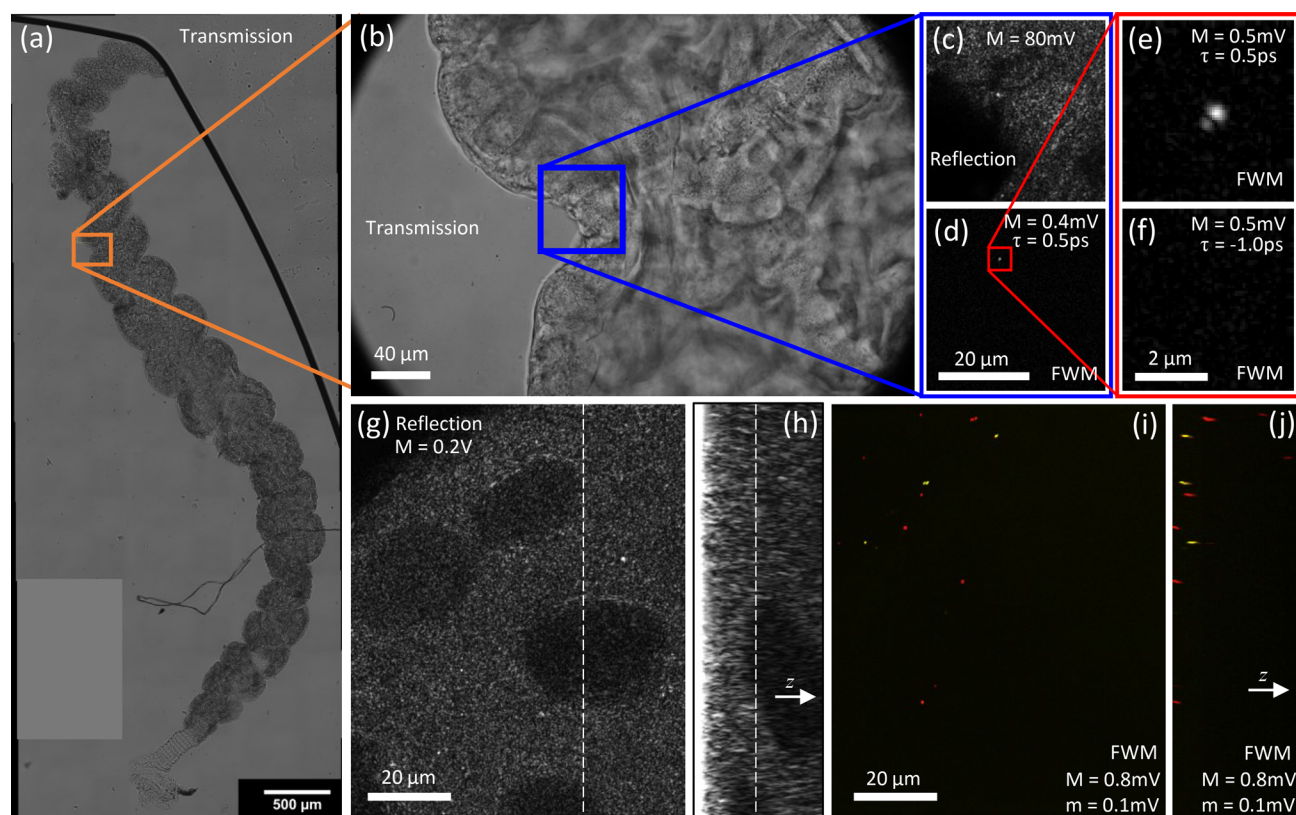
FIG. 2. 3D imaging inside the hepatopancreas of *Oniscus asellus*. (a) and (b) Bright-field transmission images; (c) and [(g) and (h)] probe reflection amplitude acquired simultaneously with the FWM amplitude in (d)–(f) and (i) and (j), respectively. (a) Stitched image (using a 10×0.3 NA dry objective) of a single HP tubule, showing the helical structure. (b) Higher magnification of the region highlighted by the orange frame in (a) taken with the 60×1.27 NA water-immersion objective also used for FWM, containing the region imaged by FWM (blue frame). (c) and (d) Reflection and FWM image ($\tau = 0.5$ ps) of the region highlighted in (b); the reflection shows the morphology the HP tubule while FWM locates AuNPs background-free. (e) and (f) Higher magnification FWM image of the region identified in (d); the FWM amplitude at $\tau = 0.5$ ps (e) is much higher than the amplitude at $\tau = -1.0$ ps (f), as expected for AuNPs. FWM images (d)–(f) are shown on a gray scale from 0 to M. (g)–(j) z-stack taken through the HP tubule over the region highlighted by the dashed light blue box shown in Fig. 1 starting at the coverslip and extending 30 μm into the tubule using a step size of 0.5 μm. Same scale bar for all, shown in (g) and (i). (g) xy reflection image at $z = 14.5$ μm, and dashed line indicates the position of line cut used to generate h. (h) yz reflection image of the HP tubule, and dashed line indicates the plane of (g). (i) and (j) Color overlay of maximum amplitude projection images of the z-stack, red channel $\tau = 0.5$ ps, and green channel $\tau = -1$ ps. Amplitude range from m to M in both the red and green channels. (i) xy maximum amplitude projection image; AuNPs (appearing in red) can be seen across the image. (j) yz maximum amplitude projection image showing the distribution of AuNPs across the z-stack. (c)–(f) Pump (probe) power at the sample was 20 μW (10 μW). (c) and (d) 0.5 ms-pixel dwell time, 40×40 μm² image with 72 nm pixel size. (e) and (f) 1.0 ms pixel dwell time, 5×5 μm² image with 70 nm pixel size. (g)–(j) Pump (probe) power at the sample was 70 μW (35 μW), 0.25 ms pixel dwell time, and the image is 100×80 μm², with 72 nm pixel size in plane.

binucleated and larger than S cells. Full z-stacks of fluorescence and DIC z-stack and their overlays are available in the supplementary material, see Table S1.

The white box indicates the region where a FWM z-stack was acquired. The simultaneously acquired reflection image in Fig. 3(b) allows a correlation of this region with the DIC image. Dashed lines indicate assumed cell boundaries. The FWM is represented as a maximum amplitude false color image [$\tau = 0.5$ ps (red) and $\tau = -1$ ps (green)] and is shown in Fig. 3(c). The blue and green dashed boxes indicate the positions of the zooms shown in Figs. 3(d) and 3(e), respectively. While the results presented here are aimed at demonstrating the capabilities of the FWM technique, they also hint toward an interesting finding from a biological standpoint. Although some AuNPs can be seen at the edges of the assumed B cells, many more are seen toward the

center of the assumed S cells. There is also more photothermal signal observed within the S cells, suggesting that the observed photothermal response arises from Cu deposits/cuprosomes contained in the S cells. Since isopods were collected during the period where B cells are thought to be accumulating metals, this finding is unexpected and interesting from a biological standpoint, suggesting a role of these cells different than previously thought. Additional data shown in supplementary material Sec. S4 are consistent with this observation, assuming the attribution to S and B cells is correct. It is of note that due to the nature of the cuprosomes inside the S cells, any other metal that accumulates within this cell is difficult to observe in XRF due to the strong signal from the Cu granules.[8] Importantly, the cytology and metallome of B cells are still not well understood. The FWM microscopy method shown here can help filling this knowledge gap.
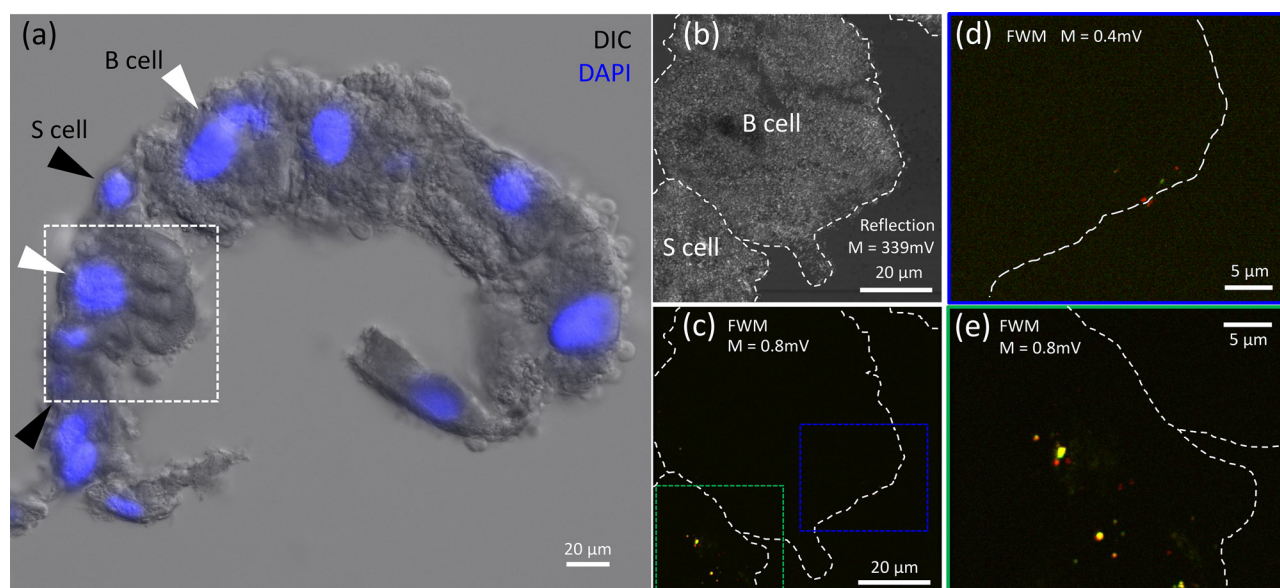
FIG. 3. Section from a HP tubule, 12 μm thick, mounted in water between a glass slide and coverslip. The nuclei have been fluorescently stained with DAPI to help identify the B and S cells. Cells are attributed to type B (white arrows) by their double nucleus and larger shape and to type S cells (black arrows) by their single nucleus and smaller shape. (a) Overlay of differential interference contrast (DIC) at 90° phase offset (gray) and wide-field fluorescence (blue) of DAPI. White arrows indicate B cells, identifiable by their double nucleus and shape, and black arrows indicate S cells. The dashed box indicates the region imaged by FWM. (b) Maximum amplitude projection of the probe reflection z-stack for the region highlighted in (a). Cell boundaries have been inferred from the reflection z-stack in the context of (a) and marked with dashed white lines. (c) False color maximum amplitude projection of the FWM z-stack for the region highlighted in (a), with $\tau = 0.5$ ps and $\tau = -1$ ps in red and green, respectively. Dashed white lines as in (b). (d) and (e) Zooms of the regions indicated by the colored dashed boxes in (c). Images are presented on a gray (color red and green) scale from 0 to M as indicated. (b) and (c) Pump (probe) power at the sample was 50 μW (25 μW), 0.5 ms pixel dwell time, 80 × 80 μm^2 image with 72 nm in the plane pixel size, and z-stacks over 7 μm in 0.5 μm z-steps.

In summary, we have demonstrated the application of FWM microscopy to locate single AuNPs of 10 nm radius in 3D inside individual cells within a multi-cellular organ of biological and environmental relevance, namely, the hepatopancreas of the terrestrial isopod *Oniscus asellus*, free from the strong light scattering background in these large (few mm) samples. AuNPs were distinguished from other metal deposits known to accumulate in this organ, owing to the physical origin and characteristic ultrafast dynamics of the transient resonant FWM technique. Considering its simplicity and 3D imaging capabilities, FWM microscopy holds great potential to complement synchrotron-based x-ray methods when investigating metal nanoparticles inside biological systems. Albeit shown here on fixed cells, FWM microscopy is applicable to living cells, paving the way to unravel the spatiotemporal journey of nanoparticles inside complex biological systems.

See the supplementary material for the details of the FWM microscope setup in Sec. S1, the sample overview imaging by DIC and fluorescence in Sec. S2, and the sample preparation in Sec. S3. Imaging results of an additional HP tubule section are given in Sec. S4, as well as movies for all imaging z-stacks.

AUTHOR DECLARATIONS
Conflict of Interest

The authors have no conflicts to disclose.

Author Contributions

Iestyn Pope: Investigation (lead); Formal analysis (equal); Data Curation (equal); Visualization (equal); Writing – Original Draft (equal); Writing – Review & Editing (equal). **Nuno G. C. Ferreira**: Investigation (equal); Resources (equal); Writing – Review & Editing (supporting). **Peter Kille**: Conceptualization (supporting); Resources (equal); Writing – Review & Editing (supporting). **Wolfgang Langbein**: Conceptualization (equal); Methodology (equal); Formal analysis (equal); Software (lead); Resources (equal); Data Curation (equal); Writing – Original Draft (equal); Writing – Review & Editing (equal). **Paola Borri**: Conceptualization (equal); Methodology (equal); Writing – Original Draft (equal); Writing – Review & Editing (equal); Project administration (lead); Funding acquisition (lead).

DATA AVAILABILITY

The data that support the findings of this study are available within the article and can also be found in the Cardiff University data catalogue at http://doi.org/10.17035/d.2023.0248427481.

REFERENCES

[1] R. Ortega, G. Devès, and A. Carmona, "Bio-metals imaging and speciation in cells using proton and synchrotron radiation x-ray microspectroscopy," J. R. Soc. Interface **6**, S649 (2009).

[2] G. Zoriniants, F. Masia, N. Giannakopoulou, W. Langbein, and P. Borri, "Background-free 3D nanometric localization and sub-nm asymmetry detection of single plasmonic nanoparticles by four-wave mixing interferometry with optical vortices," Phys. Rev. X **7**, 041022 (2017).

[3] N. Giannakopoulou, J. B. Williams, P. R. Moody, E. J. Sayers, J. P. Magnusson, I. Pope, L. Payne, C. Alexander, A. T. Jones, W. Langbein, P. Watsona, and P. Borri, "Four-wave-mixing microscopy reveals non-colocalisation between gold nanoparticles and fluorophore conjugates inside cells," Nanoscale **12**, 4622–4635 (2020).

[4] I. Pope, H. Tanner, F. Masia, L. Payne, K. P. Arkill, J. Mantell, W. Langbein, P. Borri, and P. Verkade, "Correlative light electron microscopy using small gold nanoparticles as single probes," Light Sci. Appl. **12**, 80 (2023).

[5] F. Masia, W. Langbein, and P. Borri, "Measurement of the dynamics of plasmons inside individual gold nanoparticles using a femtosecond phase-resolved microscope," Phys. Rev. B **85**, 235403 (2012).

[6] M. Hassall, J. G. Turner, and M. R. W. Rands, "Effects of terrestrial isopods on the decomposition of woodland leaf litter," Oecologia **72**, 597–604 (1987).

[7] A. Jemec, M. Kos, D. Drobne, I. K. Koponen, J. Vukić, N. G. Ferreira, S. Loureiro, and H. V. McShane, "In field conditions, commercial pigment grade TiO_2 was not harmful to terrestrial isopods but reduced leaf litter fragmentation," Sci. Total Environ. **571**, 1128–1135 (2016).

[8] P. Kille, A. J. Morgan, K. Powell, J. F. W. Mosselmans, D. Hart, P. Gunning, A. Hayes, D. Scarborough, I. McDonald, and J. M. Charnock, "Venus trapped, Mars transits: Cu and Fe redox chemistry, cellular topography and *in situ* ligand binding in terrestrial isopod hepatopancreas," Open Biol. **6**, 150270 (2016).

[9] M. H. Donker, P. Koevoets, J. A. Verkleij, and N. M. van Straalen, "Metal binding compounds in hepatopancreas and haemolymph of *Porcellio Scaber* (isopoda) from contaminated and reference areas," Comp. Biochem. Physiol. C **97**, 119–126 (1990).

[10] D. Drobne, M. Blažič, C. A. van Gestel, V. Lešer, P. Zidar, A. Jemec, and P. Trebše, "Toxicity of imidacloprid to the terrestrial isopod *Porcellio Scaber* (isopoda, crustacea)," Chemosphere **71**, 1326–1334 (2008).

[11] S. P. Hopkin, "Species-specific differences in the net assimilation of zinc, cadmium, lead, copper and iron by the terrestrial isopods *Oniscus asellus* and *Porcellio scaber*," J. Appl. Ecol. **27**, 460–474 (1990).

[12] C. A. C. Hames and S. P. Hopkin, "A daily cycle of apocrine secretion by the b cells in the hepatopancreas of terrestrial isopods," Can. J. Zool. **69**, 1931–1937 (1991).

[13] F. Masia, W. Langbein, P. Watson, and P. Borri, "Resonant four-wave mixing of gold nanoparticles for three-dimensional cell microscopy," Opt. Lett. **34**, 1816–1818 (2009).